Z. Kristallogr. Suppl. **27** (2008) 27-35 / **DOI** 10.1524/zksu.2008.0005

Optimisation of coherent X-ray diffraction imaging at ultrabright synchrotron sources

Ian K. Robinson[1,2,*]

[1] Diamond Light Source, Harwell Science and Innovation Campus, Didcot, OX11 0DE, United Kingdom
[2] London Centre for Nanotechnology, University College, Gower St, London, WC1E 6BT, United Kingdom
[*] i.robinson@ucl.ac.uk

Keywords: diffraction, coherence, imaging, nanocrystals, synchrotron radiation

Abstract. Coherent X-ray Diffraction Imaging (CXDI) is a powerful method of imaging single crystalline grains within a powder. Direct Fourier transformation of the oversampled diffraction pattern surrounding a Bragg peak is possible once the phases have been obtained using a 'support' constraint. The image is in general complex with the phase representing a projection of the atomic displacements allowing access to the internal strains inside the crystal. CXDI relies crucially on the production of a coherent beam of X-rays, which is one of the technical advances of the latest 3rd generation Synchroton Radiation (SR) sources. It is shown here how the use of a secondary source in the design of the X-ray beamline allows the coherence to be controlled continuously over a finite range without any loss of flux. The conclusions will have significant impact on instruments currently being designed at the Diamond Light Source and the new National Synchrotron Light Source (NSLS-2).

1. Imaging of crystals

Strain fields inside nanometre-size crystals can be imaged quantitatively using the method of Coherent X-ray Diffraction Imaging (CXDI) [1-5]. A coherent X-ray beam is focussed onto a nano-grained powder sample so that relatively few grains are illuminated. One of the diffraction spots of an individual grain can isolated on a Charge-Coupled Device (CCD) detector with sufficient resolution that it becomes oversampled relative to the spacing of the fringes that arise from the finite size of the grain. The angular spacing, $\Delta\theta$, of the fringes is given by the spacing formula, $\Delta\theta = \lambda / d$, where λ is the X-ray wavelength and d is the grain size. This simply requires sufficiently small pixels and sufficient distance between the sample and the detector. The diffraction pattern is recorded in three dimensions (3D) by rocking the sample through the Bragg peak and recording a sequence of frames [5].

The 3D diffraction pattern can be Fourier inverted to an image once it has been phased. The phasing method that is most widely used today is the Hybrid Input-Output (HIO) method of

Fienup [6], which repeatedly cycles back and forth between real and reciprocal spaces using discrete Fast Fourier Transforms (FFT), while applying constraints on each side. The reciprocal space constraint is the overwriting of the amplitude of the diffraction pattern, keeping the phases. The real space constraint is the cutting off of the image outside a 'support', a finite-sized region of space just big enough to contain the crystal. The method works because the diffraction pattern is oversampled relative to the spatial Nyquist frequency [7]. When there are more measurement points than image points within the support, a solution can be found. Mathematical analysis has shown that non-unique solutions in 3D are not possible in general [8], while the effects of experimental noise on the convergence are still being explored [9]. Except in the special case where the diffraction intensity function is locally symmetric about its centre (the exact Bragg point), the resulting image is a complex 3D function. It has been shown that the phase of this image at each point is equal to the scalar (dot) product of the momentum transfer vector with the local atomic displacement from the ideal crystal lattice [10,11]. This allows quantitative mapping of strain fields.

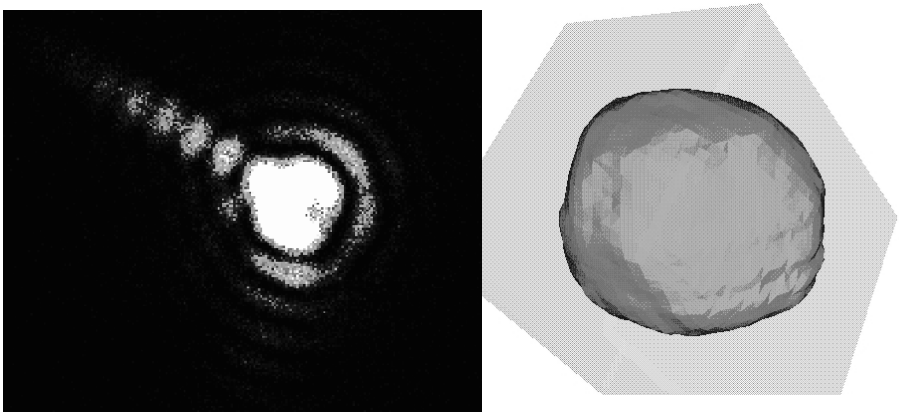

Figure 1. (a) One frame of the 3D diffraction pattern of gold crystal Au607-112, slightly off centre from the Bragg point. Circular fringes are attributed to the approximately spherical shape of the crystal, while the fringed flare on the top-left side is due to a prominent facet. (b) View of one isosurface of the inverted image of the crystal showing the expected features in the shape. A translucent image of the support used in the phasing calculation is overlaid.

An illustration of the current capabilities is shown in Figure 1. The sample is a 200nm sized crystal of gold prepared by dewetting an evaporated film of about 20nm thickness by heating in air at 1100C for about 10 hours. The substrate is the oxide layer on a silicon wafer. One issue addressed by the experiment is the extent to which the crystal becomes strained by the presence of the substrate. An analogous experiment on Pb showed a distinct pattern of strain inside the crystal that was attributed to its contact with the substrate [1]. One frame of the diffraction pattern, measured at sector 34-ID-C of the Advanced Photon Source (APS) is shown in Figure 1(a). One view of the inverted image is shown in Figure 1(b) as an isosurface (3D contour map) of the 3D density function. The phasing algorithm

was a variant of HIO in which the phase outside the support was constrained to values in the range ± π/2 [12].

2. Secondary slit for beamline optimisation

The brightness of a SR beamline arises directly from the strength of the quadrupole focussing magnets in the lattice of the storage ring and is limited by the horizontal betatron oscillations. In this paper we will ignore the vertical direction altogether, where the figures are two orders of magnitude better; at NSLS-2 the vertical direction is expected to be brightness limited in the hard X-ray part of the spectrum. The horizontal emittance, $\varepsilon = \sigma\sigma'$, is the quantity most directly relevant, where σ is the Gaussian half width of the electron source spatial distribution and σ' is the Gaussian half width of the electron source angular distribution. By Louiville's theorem applied to the electron orbit, ε is conserved around the ring, but the relative amount of the two components can vary. The ratio, $\beta = \sigma / \sigma'$ is the quantity that can be varied to match the needs of the experiments. At NSLS-2, the beta-function alternates between adjacent straight sections of the lattice. At Diamond, there are 8m 'long' and 5m 'short' straight sections around the ring with quite different beta functions. The latest-available relevant source parameters are tabulated in Table 1. There are smaller variations even within the straights, with beta rising from 10m at the end to 13m at the centre of Diamond's 'long' straight, but we will ignore these for simplicity here. Since a CXDI experiment could be implemented on any of these straights, it is necessary to choose the appropriate source parameters. The choice between these is important because it can have significant impact on the available flux and hence on the scientific outcome of the beamline.

Table 1. Design parameters for the two storage rings considered in this paper. Derived quantities refer to the symbols defined in the text.

	units	NSLS-2 Low-beta	NSLS-2 High-beta	Diamond Short	Dimond Long
σ	μm	28	99	122.9	178.4
σ'	μ-rad	19	5.5	24.2	16.5
σ_x'	μ-rad	25.30	17.58	29.40	23.48
ε	nm-rad	0.53	0.54	2.97	2.94
ε_x	nm-rad	0.71	1.74	3.61	4.19
β	m	1.47	18.00	5.08	10.81
D_1	m	150	150	250	250
D_2	m	25	25	25	25

Option I : direct use of source

s_1	µm	268	76	102	70
Coh frac		0.035	0.014	0.007	0.006

Option II: secondary slit at source

s_1 min	µm	268	76	102	70
s_1 max	µm	7589	5275	14701	11738

Option III: secondary slit at shield wall

C_{min}	µm	110	110	105	105
s_1 min	µm	-	83	107	72
s_1 max	µm	-	907	2105	3140

While the conserved emittance is defined for the electron beam, the generated X-rays no longer obey this simple conservation law. The reason is that there is a finite opening angle for the radiation emitted as it passes through an undulator, located in one of the straight sections of the ring. An electron passing through an undulator emits a radiation cone of half width [13], $1/\sqrt{N}\gamma$, where γ is the relativistic factor, 6000 for both 3GeV rings considered here, and N is the number of magnetic poles in the undulator, which we will take to be 100. The X-ray opening angle is then 16.7mrad. This opening angle has to be combined (quadratically) with the electron beam divergence to give the X-ray divergence σ_X'. As Table 1 shows, the product of X-ray source size and X-ray divergence, which we define as the "X-ray emittance" ε_X, now does vary around the ring. All numbers quoted in this paper are calculated for λ=0.1nm or 12 keV energy, which is typical for coherence-based diffraction experiments. The table shows there is a natural advantage of using the low-beta straights at NSLS-2 or the short straights at Diamond for their smaller X-ray emittance, which translates into a larger coherent flux, as seen below. The difference is more than a factor of two for NSLS-2.

Coherence-based experiments require that only part of the beam can be used. An aperture must be introduced into the beamline to limit the spatial extent of the beam to approximately one lateral coherence length. Exceptions can be made, for example in X-ray Photon Correlation Spectroscopy (XPCS), where the best signal-to-noise is found to occur for a slit size nearer to two coherence lengths [14]. The lateral correlation length of a wavefield at position P is defined from the van Cittert-Zernike theorem [15] as,

$$\xi = \lambda D / 2\sigma \qquad (1)$$

where D is distance from the source to point P. Multiplicative factors close to unity that arise from the exact distribution of the source have been omitted here and elsewhere in this paper. Once a coherent part of the wavefield has been selected by the aperture, the beam can then be manipulated using optics to concentrate it onto a small sample [16]; perfect optics will not affect

the degree of partial coherence, in principle. This paper will focus on the issues associated with the choice of aperture needed to define the coherence and not discuss the following optics further, simply assuming that one coherence length is required.

3. Design options

In both the Diamond and NSLS-2 projects, the option of 'long' beamlines for CXDI, extending outside the storage ring building, is being considered seriously. In neither case are the distances decided, but typical estimates of the position of the experiment and its coherence-defining entrance slit are given in Table 1, D_1=150m for NSLS-2 and 250m for Diamond. The conclusions of the paper are not very sensitive to the exact choice.

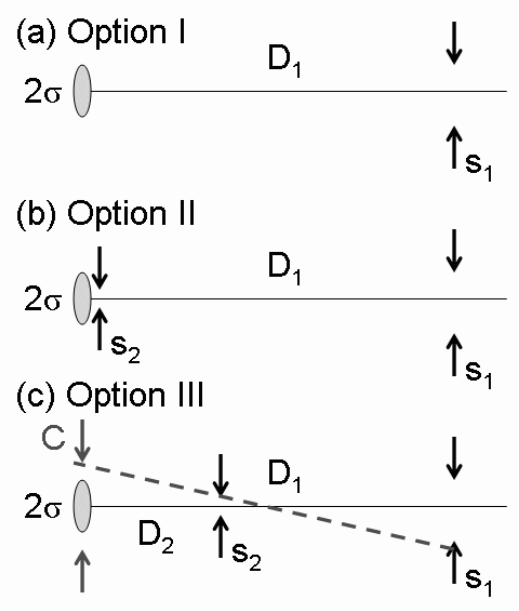

Figure 2. Schematic beamline layouts for consideration of secondary slits.
(a) Option I where the coherence at the location of the experiment entrance slit, s_1, is set by the synchrotron source itself. (b) Option II where a secondary slit is introduced at the source. (c) Option III where a secondary slit is introduced at the synchrotron shield wall. The dashed line is the ray-tracing discussed in the text to determine the projected size, C, of the slits onto the source.

The simplest option, denoted option I in Figure 2(a), is to place nothing in the beam, except perhaps windows and a monochromator that do not affect the light propagation in principle. The coherence-defining horizontal slit is then set to one coherence length, given by Equation 1 with $D=D_1$, the position of the experiment. The resulting slit/beam size, $s_1=\xi$, given in table 1, is in the range of 100 microns. This coherent beam can then illuminate the sample directly or be manipulated with optics to match the sample. In any case, the useful flux is given by the fraction

of the X-ray opening angle subtended by the slit. Assuming this to be a small fraction of the divergence, we can write this as the coherent faction of the total flux,

$$f = \frac{s_1 / D_1}{2\sigma_X'} = \frac{\lambda}{4\sigma\sigma_X'} = \frac{\lambda}{4\varepsilon_X} \quad (2)$$

As can be seen, this depends only on the X-ray emittance. It is immediately obvious that this option favours the lowest possible beta for the storage ring because of the compounding effect of the X-ray opening angle on the horizontal divergence. The coherent fraction, calculated in Table 1 to be at most a few percent of the full beam, shows that the low-beta straight at NSLS-2 gives more than a factor of two more flux than the high-beta straight for this reason.

Option II in Figure 2(b) is a hypothetical variation showing the simplest kind of secondary source. Although obviously impractical, a secondary slit of width s_2 is placed directly on top of the electron source to limit its spatial extent. The value of s_1, again equal to one coherence length of the source, now defined by s_2, is given by $s_2 = \lambda D_1 / s_1$ and tabulated in table 1, is bigger than before and can indeed be made arbitrarily large. However the resulting coherent fraction,

$$f = \frac{s_1 / D_1}{2\sigma_X'} \times \frac{s_2}{2\sigma} = \frac{\lambda}{4\varepsilon_X} \quad (3)$$

is exactly the same as before. This shows the basic principle of the secondary source, the ability to manipulate the coherence beam size without cost in flux. The two limits on the range of values of s_1, listed in table 1, are given by the constraints that the secondary slit s_2 must be smaller than the source, $s_2<2\sigma$, and that the coherence defining slit s_1 must be filled by the X-ray divergence, giving $s_1<2D_1\sigma_X'$. This gives a wide range of adjustable coherence lengths that do not reduce the coherent flux.

Option III in Figure 2(c) is the practical version of the secondary source located at the closest accessible position in the beamline, the distance of the shield wall that isolates the storage ring from the experimental hall, D_2. A slit of width s_2 is placed at distance D_2 to determine the coherence length at the experiment. This acts as a virtual source in the sense that each point within the secondary slit is incoherently illuminated by multiple overlapping waves from the actual source. The coherence-defining slit at the experiment, s_1, selecting one coherence length, is again given by Equation 1, but now with $D=(D_1-D_2)$ and 2σ replaced by s_2., giving

$$s_1 = \lambda(D_1 - D_2) / s_2 \quad (4)$$

Like with option II, a range of coherence lengths can be achieved. Within that range, as discussed below, the coherent flux is unchanged from the expression in Equations (2) and (3). Deriving this is a little harder than before; it has been verified in the special symmetric case of $s_1/D_1=s_2/D_2$ but is expected to be generally true by the Louiville theorem.

Ray tracing is needed to find the working range of values of the slit sizes s_1 and s_2 that preserve the ideal coherent flux. For simplicity, we assume box-shaped (instead of Gaussian) functions for the spatial and angular distributions; only the extreme choices for s_1 and s_2 are likely to be much affected by this assumption. It turns out that the angular distribution is sufficiently wide

that it is never a constraint. The critical ray that limits the range, shown in colour in figure 2(c), passes the extremes of the two slits and must stay within the source. The equation for this is,

$$C = s_1 \frac{D_2}{D_1 - D_2} + s_2 \frac{D_1}{D_1 - D_2} \leq 2\sigma \tag{5}$$

where the quantity C on the left-hand side of the inequality is the back-projected image of the slits and depends on both slit settings and their distances. C can be reduced to a function of a single variable by inserting the relation (4) above between s_1 and s_2 determined by the one-coherence length criterion. Expressed in terms of s_1,

$$C(s_1) = s_1 \frac{D_2}{D_1 - D_2} + \frac{\lambda D_1}{s_1} \tag{6}$$

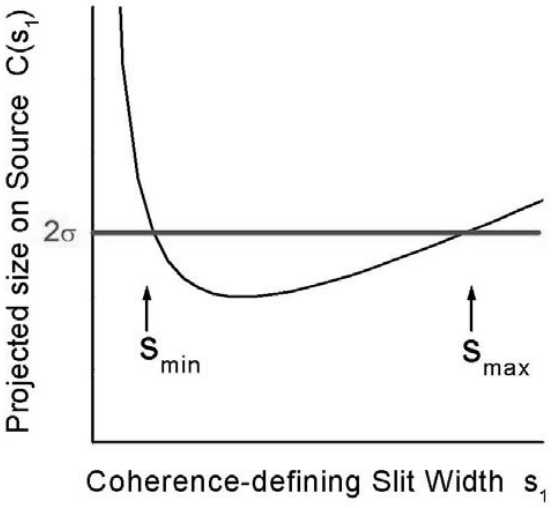

Figure 3. Variation of the projected size, C, of the slits onto the source (see Figure 2(c)) as a function of the final slit size s_1, subject to the constraint that the coherence size s_1 is set by the secondary slit s_2.

This expression is plotted in figure 3. The minimum value of $C(s_1)$, given by $C_{\min} = 2\sqrt{\frac{\lambda D_1 D_2}{D_1 - D_2}}$, is tabulated in Table 1. When $C(s_1)$ falls below the source size, 2σ, the ray-tracing condition is satisfied and we have a viable configuration with a fully illuminated secondary source. But $C(s_1)$ rises on both sides giving a limited range of allowed slit settings. The values of s_1 bounding the allowed range are,

$$s_{\max/\min} = \frac{D_1 - D_2}{D_2} \left\{ \sigma \pm \sqrt{\sigma^2 - \frac{\lambda D_1 D_2}{D_1 - D_2}} \right\} \tag{7}$$

also tabulated for the various sources in Table 1. It is notable that there is no solution for the otherwise attractive low-beta option at NSLS-2: C_{min} is already greater than the source size. In order to obtain any solution, the secondary slit must be brought forward to D_2=7.45m. In the other three cases a useful range of values is apparent. The geometric mean of s_{max} and s_{min}, also listed, is the natural centre of the two ranges. This corresponds to the symmetric choice of $s_1/D_1=s_2/D_2$ mentioned above.

4. Conclusions

The technique of CXDI is illustrated as producing a 3D image of a 200nm Au nanocrystal. The phasing was achieved by a phase-constrained HIO algorithm using oversampled 3D diffraction data. The CXDI method depends on coherence of the X-ray beams used. It will be more powerful with the production of higher fluxes in the coherent beams at the new 3rd generation SR sources. The development of suitable X-ray optics to match the sample size to the coherent beam size, which is a subject outside the present discussion, will clearly profit from the ability to adjust the size of the incoming coherent beam. It is shown here that the introduction of a secondary slit at the position of the shield wall allows control of the coherent beam sizes without cost of flux. The available range of sizes depends on the source and the layout of the beamline, but excludes the low-beta option for NSLS-2.

The main advantage of using a secondary slit is the continuous control of coherent beam size, but there are other advantages also. Because the secondary source is at an accessible location and because only a small fraction of the source is subtended by the slit, the beam may be multiplexed into multiple branches operating in parallel. This can be achieved using mirrors as done presently at 34-ID and 8-ID of APS, or else using crystal optics. The multiplexing option would be possible to implement at Diamond or NSLS-2, but only on the high-beta straights of the latter. Another advantage is that it sets the coherence outside the storage ring without reliance on a stable source of the correct size. It therefore offers immunity to instabilities of the source which would lead to a drop in flux rather than loss of coherence.

References

1. Pfeifer, M.A., Williams, G.J., Vartanyants, I.A., Harder, R. & Robinson, I.K., 2006, *Nature*, **442**, 63.
2. Harder, R., Pfeifer, M.A., Williams, G.J., Vartaniants, I.A. & Robinson, I.K., 2007, *Phys. Rev. B*, **76**, 115425.
3. Williams, G.J., Pfeifer, M.A., Vartanyants, I.A. & Robinson, I.K., 2006, *Phys. Rev. B*, **73**, 094112.
4. Robinson, I. & Miao, J., 2004, *Mat. Sci. Bull.*, **29**, 177.
5. Williams, G.J., Pfeifer, M.A., Vartanyants, I.A. & Robinson, I.K., 2003, *Phys. Rev. Lett.*, **90**, 175501-1.
6. Fienup, J.R., 1987, *J. Opt. Soc., Am. A.*, **4**, 118.
7. Sayre, D., 1952, *Acta Cryst.*, **5**, 843.

8. Bates, R.H.T., 1982, *Optik*, **61**, 247.
9. Williams, G.J., Pfeifer, M.A., Vartanyants I.A. & Robinson, I.K., 2007, *Acta Cryst*., A**63**, 36.
10. Robinson , I.K. & Vartanyants, I.A., 2001, *Appl. Surf. Sci.*, **182**, 186.
11. Vartanyants, I.A. & Robinson, I.K., 2001, *J. Phys. : Condens. Matter*, **13**, 10593-611.
12. Harder, R., to be published.
13. Als-Nielsen, J. & McMorrow, D., 2001, *Elements of Modern X-ray Physics* (Wiley).
14. Sandy, A., private communication.
15. Born, M. & Wolf, E., 1999, *Principles of Optics: Electromagnetic Theory of Propagation, Interference and Diffraction of Light* (Cambridge: University Press), 7th edition.
16. Robinson, I.K., Pfeiffer, F., Vartanyants, I.A., Sun Y. & Xia, Y., 2003, *Optics Express*, **11**, 2329.

Acknowledgements. The author wishes to thank Ulrich Wagner, Christoph Rau, Scott Coburn and Lonny Berman for valuable discussions about the latest developments at the two new SR sources. Ross Harder assisted with the measurements and his phase constrained HIO algorithm [12] was used for inversion of the data in Figure 1. The experimental work was carried out at the Advanced Photon Source (APS) beamline 34-ID-C, which was operated by the Materials Research Laboratory of the University of Illinois under DOE contract DEFG02-91ER45439. APS is operated by DOE contract No W 31 109 ENG 38. This research was supported by the EPSRC.